Spanning spatiotemporal scales with simultaneous mesoscopic Ca^{2+} imaging and functional MRI

Evelyn MR Lake*, Xinxin Ge†, Xilin Shen, Peter Herman, Fahmeed Hyder, Jessica A. Cardin, Michael J. Higley, Dustin Scheinost, Xenophon Papademetris, Michael C. Crair❖, & R. Todd Constable❖

* Corresponding author
† Equally contributing co-first author
❖ Jointly supervised the research

ABSTRACT

Neuroscience encompasses the investigation of brain function across multiple spatiotemporal scales. Yet, most research is confined to one spatiotemporal milieu limiting the integration of knowledge across scales. Here we describe an imaging and analytic approach that spans spatiotemporal scales by combining simultaneous wide field mesoscopic 1-photon Ca^{2+} imaging and functional magnetic resonance imaging (fMRI) at 11.7T. Given the confined space within the magnet, that metal is prohibited, and the unique/conflicting needs of each methodology, these techniques have never before been combined. In addition to describing the new hardware and software, we present evoked and spontaneous activity measurements made in lightly anesthetized animals. We have three findings: (1) for both evoked and spontaneous activity the magnitude of the Ca^{2+} and fMRI signals show correspondence, (2) connectivity matrices derived from Ca^{2+} and fMRI measurements are stable throughout an imaging session, and (3) there is correspondence between Ca^{2+} and fMRI spontaneous activity patterns.

INTRODUCTION

The present work details the design and preliminary testing results of an imaging technology that combines wide field 1-photon optical imaging of the full cortical surface with whole-brain functional magnetic resonance imaging (fMRI). We describe the novel hardware and software developed for simultaneous imaging with these modalities. Furthermore, we present results from data collected using transgenic mice with excitatory neurons labeled with fluorescent Ca^{2+} (GCaMP6). Together these wide-field Ca^{2+} imaging data and the blood oxygen level dependent (BOLD) fMRI data provide two indirect measures of ground truth neuronal activity.

Specifically, the Ca^{2+} fluorescence signal is a mesoscopic measure of local changes in intracellular Ca^{2+} concentration. Whereas, the BOLD signal arises from changes in the paramagnetic properties of hemoglobin which occur when there are local changes in blood flow and volume in response to metabolic demand [Ogawa1992]. Although the BOLD signal is an indirect measure, it is an endogenous source of contrast, which is easily collected from the whole brain, and it is a measurement amenable to studies in research animals as well as human subjects. By combining wide-field 1-photon Ca^{2+} and BOLD imaging we create a tool which spans spatiotemporal scales that will provide a firmer biological basis for informing our understanding of the functional organization of the brain.

Simultaneous imaging of brain function using multi-modal approaches has been reported previously. Notably, the combination of fluorescence imaging techniques (typically using a single fiber optic cable) with fMRI [Schulz2012, Liang2017, Schwalm2017, Albers2018, Schlegel2018, Wang2018], and the combination of wide-field Ca^{2+} and intrinsic hemodynamic signal measurements (as a substitute for the BOLD signal) [Ma2016, Murphy2018, Gu2018]. What is unique and powerful about the present combination, is the spatial coverage of both modalities.

Where previous studies that included fMRI have surgically implanted no more than a couple optical fibers for fluorescence recordings [Schulz2012, Iordanova2015, Duffy2015, Schmid2016, Cui2017, Liang2017, Schwalm2017, Albers2018, Schlegel2018, Wang2018], we use a telecentric lens and coherent optical fiber array containing over one million fibers with a 1.45cm^2 field of view (FOV). This allows imaging coverage of most of the cortical surface allowing network and systems level measurements that previous methods could not provide.

Previous work using hemodynamic signal measurements instead of fMRI, lack whole brain coverage [Ma2016, Murphy2018, Gu2018]. Thus these techniques are unable to gain insight into relationships between cortical activity and deeper brain structures. Furthermore, the approximation of the BOLD signal by intrinsic hemodynamic signal measurements is an active area of study [Hillman2014] which we circumvent in the present work. However, the technology described here can be used to measure the intrinsic hemodynamic signal simultaneously with BOLD and Ca^{2+} imaging. Thus, our device could be used to investigate the relationship between the intrinsic hemodynamic signal, BOLD and Ca^{2+} physiologic changes.

Several challenges were overcome to develop our dual imaging apparatus and analysis pipeline. Notably, due to the high magnetic field environment metal components had to be eliminated from the apparatus or housed outside the magnet room. Furthermore, the magnet generates significant vibrations while collecting data which can cause motion artifacts in both fMRI and Ca^{2+} recordings. In addition, the co-registration of the Ca^{2+} data (a 2D surface) and the fMRI data (a 3D volume) is a non-trivial image registration problem for which we developed new software (now available online www.bioimagesuite.org). How these (and other) challenges were overcome are described in Results Sections I., II. & III.

In addition, we present results from our preliminary testing of the sensitivity and stability of the simultaneous recordings. First, we examine the correspondence between response amplitude fluctuations in the magnitude of the Ca^{2+} and BOLD evoked responses to hind-limb stimulation [section IV.]. Second, using spontaneous activity, we introduce data driven parcellation; an analysis method adapted from the human resting-state fMRI literature [Shen2010, vanOort2018, Arslan2018, Eickhoff2018] which uses a multi-graph k-way clustering algorithm to identify functional brain regions [Shen2013]. We apply this method using either the Ca^{2+} or BOLD data [section V.]. The temporal stability (throughout the duration of an imaging session) was also measured for the connectivity matrices obtained from the Ca^{2+} and BOLD modalities (a measure of activity synchrony between regions) [section VI.]. Third, we measure the correspondence between Ca^{2+} and BOLD patterns of spontaneous activity [section VII.].

RESULTS

I. Set-up for simultaneous mesoscopic Ca^{2+} imaging and fMRI

We have designed and built an apparatus that enables the simultaneous collection of fluorescent Ca^{2+} signal from the whole cortical surface and fMR-imaging of the whole brain. A schematic of the experimental set-up is shown in Figure 1.a. We conduct through-skull optical signal acquisition, which necessitates a brief and minimally invasive surgical preparation optimized

for dual imaging (Methods, below I.). Briefly, following scalp resection, a dental cement 'well' is built along the circumference of the skull surface. The well is filled with an MRI compatible, optically transparent material (Phytagel), and sealed with a glass cover-slip and dental cement. The skull preparation is fixed to a custom (3D printed) head holder which dovetails with an in-house built MRI coil (hardware for MRI-signal reception) and the optical imaging equipment. A photograph of a prepared mouse is shown in Figure 1.b, and a photograph of the assembled dual imaging apparatus is shown in Figure 1.c.

The mouse, secured to the custom head-plate, rests beneath the MRI saddle coil (Supplementary Figure 1). The saddle coil configuration is ideally suited for dual imaging as it does not obstruct the optical FOV, has uniform whole-brain MR-sensitivity, and is relatively easy to build (allowing customization for different animal sizes). The hardware components for Ca^{2+} imaging are secured above the MRI coil using custom 3D printed parts (Methods, below II.).

All together, the dual imaging set-up is assembled within an 8cm diameter plastic sled (Cast Acrylic, McMaster-Carr) which inserts into the 11.7T preclinical Bruker magnet. Notably, this design (for an exceptionally small bore size) can be easily scaled for larger animals and bore sizes. In sum, the components necessary for the dual imaging experiment (with the exception of the magnet) amount to less than $60,000.

II. Multi-modal image acquisition

We collect fluorescence signal from the full cortical surface using a fiber-optic bundle which contains one million fiber-optic cables. A photograph of the fiber-optic bundle as well as a single-frame raw fluorescence image captured using this set-up is shown in Figure 1.d. Similarly, raw fMR-images and the corresponding structural MR-images are shown in Figure 2.a.iii.

In the present work, we image transgenic mice expressing GCaMP6f in excitatory neuronal cell populations (Methods, below III.). However, it should be emphasized that the methods and techniques we describe here can be implemented using **any** mouse line with sufficiently bright optical signal (eg. different cellular populations or even voltage indicators). Furthermore, this apparatus can also be used to measure the intrinsic hemodynamic signal.

During data acquisition, mice were minimally anesthetized with 0.5-1.25% Isoflurane, adjusted to maintain a heart rate of 480-550 beats per minute (bpm). In the present work, anesthesia was used to avoid complications inherent to imaging awake animals in the MRI environment (e.g. training, motion, and stress). However, our experiment is designed with the goal of conducting awake animal experiments in the future. Thus, the dual imaging apparatus, surgical procedure, and imaging protocol are compatible with longitudinal imaging as well as awake animal experiments.

Animals were free breathing a mixture of O_2 and medical air, adjusted to maintain an arterial O_2 saturation of 94-98%. Heart and breath rate, arterial O_2 saturation, and rectal temperature, were continually monitored (MouseOx from STARR) and recorded (Spike2, Cambridge Electronic Design Limited) Supplementary Figure 1. Body temperature was maintained with a circulating water bath. During image acquisition, MRI, Ca^{2+} imaging and physiological data recording were all synchronized (Master-8 A.M.P.I., Spike2 Cambridge Electronic Design Limited).

Fluorescence and fMR-imaging parameters are detailed in Methods, below IV. Briefly, the acquisition of every 20 Ca^{2+} imaging frames (20Hz acquisition rate with every other image used for background correction, refer to Methods, below V.) is triggered by the collection of each fMRI volume (ie. whole brain image obtained once per second, TR=1000ms). From the fiber-optic bundle, we obtain a spatial resolution of 25μm^2 and a 1.45cm^2 FOV containing the whole cortical surface. Functional MRI data from the whole brain is acquired at 1Hz with a spatial resolution of

0.4mm^3. Additional structural MRI data is acquired for multi-modal image registration (next section). We record both evoked responses to unilateral hind-paw stimulation, as well as spontaneous activity. Fluorescence and fMRI data are processed using standard procedures (e.g. motion correction, bandpass filtering, drift correction and global signal regression), refer to Methods, below V. & VI.

III. Multi-modal image registration

To move the simultaneously recorded Ca^{2+} (2D-surface) and MR (3D-volume) images into the same space is a non-trivial image registration problem (Figure 2). We accomplish this task using the anatomy of the vasculature on the surface of the cortex, which is visible in the optical images and can be visualized by collecting a MR-angiogram without the need for an exogenous contrast agent.

All image registration is performed using BioImageSuite Web, a software package developed in-house for this purpose and available online (www.bioimagesuite.org). For multi-modal image registration (Figure 2.b.), in addition to the Ca^{2+} (1) and fMRI (2) time-series data, we require an average Ca^{2+} image (mean across all frames, ImageJ *mean*), a high in-plane resolution anatomical MR image matching the fMR-image prescription (T_2 multi-slice-multi-echo, MSME) (3), an isotropic high-resolution MR anatomical image of the whole brain (T_2 MSME) (4), an MR-angiogram (T_1 fast-low-angle-shot, FLASH, time-of-flight, TOF) (5), and a high-resolution image of the brain tissue within the MR-angiogram FOV (T_1 FLASH) (6). See Methods, below IV. and VII. for imaging parameters.

A schematic of the multi-modal registration protocol is outlined in Figure 2.b. Brain-masks are applied to all data using signal intensity thresholding for skull and surrounding tissue signal removal. Next, the high in-plane resolution anatomical images which match the fMRI scan prescription (3) are registered to the fMRI data (2) and to the isotropic high-resolution anatomical image (4) using a rigid registration algorithm that employs the normalized mutual information metric [Studholme1996]. Likewise, the high-resolution image of the brain tissue within the MR-angiogram FOV (6) and the MR-angiogram (5) are registered to the high-resolution anatomical image (4). These steps move all the MRI data into the 'animal's reference space'. Using the isotropic high-resolution anatomical image (4), the data from each animal can be moved to an atlas (such as the The Allen Brain Atlas http://www.brain-map.org) or any other reference space using a non-linear, non-rigid registration method again based on normalized mutual information [Rueckert1999, Papademetris2003].

Next, we use a custom ray-casting algorithm on the masked angiography image (Figure 2.c.i.) to create a 2D projection image (Figure 2.c.ii.). This algorithm projects rays from the top of the image and uses the brain surface normal for shading to create a synthetic brain surface image (Supplementary Figure 5. & Supplementary Material I.). This effectively projects the MR into the same space as the Ca^{2+} data which is viewed from above. This image contains anatomical details (e.g. cortical surface vessels) that are also visible in the average Ca^{2+} image. For each mouse, anatomical features present in both images, such as the projections of the middle cerebral arteries and the midline, are used to generate a rigid transformation that brings the Ca^{2+} and MRI data into alignment (Figure 2.c.iv.).

IV. The magnitude of individual evoked Ca^{2+} responses is related to the magnitude of the same individual evoked BOLD responses independent of stimulus modulation

Previous work has demonstrated that the magnitude of the Ca^{2+} and BOLD responses change in synchrony when modulated by changing stimulus parameters (i.e. larger/smaller elicited Ca^{2+} changes co-occur with larger/smaller BOLD signal changes) [Schulz2012]. In the present work, a constant current and frequency unilateral hind-paw stimulation protocol (1mA, 5Hz, 5/55 seconds ON/OFF) is used to probe for a relationship between the magnitudes of Ca^{2+} and BOLD responses. Furthermore, by recording Ca^{2+} signal from most of the cortical surface, we can use a data driven approach to identify the responding Ca^{2+} ROI. Thus, we define responding ROIs from Ca^{2+} and BOLD data using generalized linear modeling (GLM, Methods, below VIII.) Supplementary Figure 7.

To quantify individual response amplitudes we average the signal within the responding ROI from the peak of the response until three seconds after the peak. The peak of the response is defined using the time-to-peak (TTP), calculated from one run (9 stimulations) for each of six mice (Ca^{2+} TTP: 0.6 ± 0.03 seconds, and BOLD TTP: 4.7 ± 0.5 seconds, mean ± standard deviation, SD), Supplementary Figure 8. We find that spontaneous Ca^{2+} and BOLD individual response amplitudes are moderately correlated (Pearson's correlation), $R=0.28$ $P<0.04$, Figure 3. Given that individual responses are noisy, and that spontaneous fluctuations have a small effect size, a moderate correlation is expected. Furthermore, as the Ca^{2+} and BOLD signals fundamentally measure different correlates of the neuronal response a high level of correspondence is not expected. Indeed, if these metrics were too well matched, it could be argued that simultaneous measurements are unnecessary. Finally, it should be emphasized that this relationship could not have been observed without stable simultaneous multi-modal data acquisition.

V. Functional parcellation of Ca^{2+} and fMRI spontaneous activity

Functional connectivity can be studied with the simultaneous acquisition of Ca^{2+} and fMRI data to investigate fundamental questions regarding brain-wide circuit connectivity. To perform connectivity analyses we require an atlas of nodes. This can be obtained from anatomic data (for example, from the Allen atlas) but in some cases a functional atlas is preferable. With functional data, the correlation between the average time courses from two nodes is taken as a measure of the strength of the connection (i.e. the functional connectivity) between nodes. Such a connection in graph theory is referred to as an edge. A map of connectivity strength (i.e. connectivity between all pairs of nodes or along all edges) is a measure of functional brain organization.

In human fMRI research, functional parcellation and connectivity mapping using spontaneous activity (i.e. BOLD imaging in the absence of a task or elicited response) has received much attention [Buckner2009, Shen2010, Brown2011, Cao2011, Yao2010, Sanz-Argita2010, Wang2012, Venkataram2012, Craddock2012]. In the present work, we apply functional parcellation and connectivity analyses to Ca^{2+} and BOLD data. Using a multi-graph k-means clustering approach [Shen2013, www.nitrc.org/frs/?group_id=51] we generate a data-driven functional brain atlas using either modality. For algorithm details refer to Methods, below IX., and Supplementary Figure 9.

VI. For Ca^{2+} and BOLD, connectivity patterns are stable throughout data acquisition

We collect 50 minutes of resting-state Ca^{2+} and fMRI data from 6 mice, in five 10 minute acquisitions spread over the course of a 2.5 hour study. This data is used to calculate individualized parcellations from the Ca^{2+} Figure 4.a. and fMRI Figure 4.b. data. In order to assess the stability/repeatability of the connectivity data, we applied the parcellation atlas to each 10 minute run separately in order to generate a the connectivity matrix for each run, thereby yielding 5

connectivity profiles for each animal, from each modality. By computing the correlation of the connectivity patterns across time (Figure 4.c/d.), we obtain a measure of connectivity profile stability during our experiment. We find that the patterns of Ca^{2+} and BOLD connectivity are very stable. If we convert each connectivity matrix to a vector and use Pearson correlation to measure the similarity of these connectivity matrices we find across mice: Ca^{2+} R=0.995 ± 0.003, and BOLD R=0.84 ± 0.09 (mean ± SD).

VII. Ca^{2+} and BOLD share similar parcellation topology and connectivity patterns, yet there is a stronger relationship between Ca^{2+} and BOLD connectivity when the parcellation is determined using BOLD data

For each mouse, we compute a parcellation using Ca^{2+} data and a parcellation using BOLD data. With our multi-modal data in the same space, we transpose the Ca^{2+}-parcellation onto the BOLD data, and the BOLD-parcellation onto the Ca^{2+} data (Figure 5.a.), and examine parcel topology and connectivity patterns. On average, a parcellation based on either Ca^{2+} or BOLD data results in qualitatively similar topological patterns. Broadly, the data driven parcellations reliably identify motor, retrosplenial, primary somatosensory, visual and auditory regions (Supplementary Figure 10). Likewise, the connectivity patterns observed in Ca^{2+} and BOLD data, when a Ca^{2+} or BOLD parcellation is imposed, appear similar (Figure 5.b.).

We observe that regions within hemispheres that are more highly correlated are neighbouring rather than distant. Furthermore, within hemisphere BOLD connectivity strength is greater (mean R=0.20) than between hemisphere connectivity strength (mean R=0.10), $P<0.05$, whereas within and between hemisphere Ca^{2+} connectivity strength is equal (mean R=0.67), $P>0.1$. Finally, bilaterally paired regions (e.g. primary somatosensory areas in the right and left hemispheres) are more highly correlated than mismatched regions (e.g. primary somatosensory and visual areas). These observations are evident whether the parcellation is made using Ca^{2+} or BOLD data.

To quantify the similarity between Ca^{2+} and BOLD spontaneous activity patterns, we compute the correlation between Ca^{2+} and BOLD connectivity (Figure 5.c.). For both Ca^{2+} and BOLD parcellations, inter-/intra-hemisphere and whole brain connectivity patterns show a relationship between modalities. In other words, regions which show high/low synchrony in Ca^{2+} data also show high/low synchrony in BOLD data. Notably, the correlation between Ca^{2+} and BOLD connectivity strength is greater when the parcellation is calculated using BOLD data than when the parcellation is calculated using Ca^{2+} data.

DISCUSSION

In the present work we describe the design and development of a novel imaging device that combines mesoscopic 1-photon Ca^{2+} imaging and simultaneous fMRI in a transgenic mouse model. New hardware and software were needed to enable the collection and analysis of these data. The method described here can be duplicated by fellow researchers. Furthermore, we present three preliminary findings obtained using the dual imaging device: (1) correspondence between activation amplitudes and spontaneous fluctuations in the Ca^{2+} and BOLD signals, (2) stability of Ca^{2+} and BOLD connectivity matrices across the duration of an imaging session, and (3) correspondence between Ca^{2+} and BOLD patterns of spontaneous activity.

The simultaneous recording of Ca^{2+} and BOLD data has been reported previously [Schulz2012, Liang2017, Schwalm2017, Albers2018, Schlegel2018, Wang201] but with limited spatial coverage (only a single optical fiber was used to record time series from an ROI). In the

present work, we use over one million fibers to record Ca^{2+} data from the cortical surface. This increase in spatial coverage enables multi-modal data to be used to probe systems neuroscience questions on the fundamentals of brain function and organization. Examples from the present work include: using a GLM to identify the Ca^{2+} ROI responding to hind limb stimulation, and analyses of spontaneous activity.

The BOLD signal is correlated with hemodynamic changes which can be measured [Ma2016, Murphy2018, Gu2018]. This emerging body of work is an excellent resource to which simultaneously collected Ca^{2+} and BOLD data (present work) can be compared. Furthermore, future work with our device can add to this body of work through the simultaneous collection of intrinsic hemodynamic and Ca^{2+} signal from the cortex, and BOLD data from the whole brain.

To introduce simultaneous mesoscopic Ca^{2+} and BOLD imaging, we show three results chosen to demonstrate sensitivity and stability. To test sensitivity we measure the correspondence between spontaneous fluctuations in the magnitude of Ca^{2+} and BOLD evoked responses. We show that for ROIs defined by each modality, there is moderate correspondence between Ca^{2+} and BOLD response magnitudes when stimulus parameters are held constant. Next, we examine the stability of Ca^{2+} and BOLD connectivity using recordings of spontaneous activity distributed throughout the duration of the imaging session. We find that across 2.5 hours of imaging, the Ca^{2+} and BOLD connectivity profiles (based on 10 minute samples) remain very stable. Finally, we measure the correspondence between Ca^{2+} and BOLD in their spontaneous activity patterns. We observe that these patterns show spatial as well as functional moderate-high correspondence between modalities. In summary, our results indicate a satisfying level of sensitivity, good stability, and some promising preliminary relationships between the simultaneously recorded Ca^{2+} and BOLD signals.

The main limitation of the present work, is that all recordings were acute and performed in anaesthetized animals. Anaesthetics are known to have profound effects on brain activity [Gao2017] which limits the scope of the present findings. However, given the known complications inherent to imaging awake animals in the MR environment, we chose to perform all our initial experiments using 0.5-1.25% isoflurane. To address this limitation, we have begun to develop and test a chronic surgical preparation for longitudinal imaging in awake animals. To this end, all the features of the device described here are compatible with this endeavour.

The hardware and software developments presented here are broad and generalizable. This technology is not limited to measuring Ca^{2+} signals and fMRI. As mentioned above, the hemodynamic signal can also be measured. Furthermore, we are able to quantify the contributions of different cell populations (e.g. excitatory neurons, inhibitory neurons and glial cells) to the BOLD signal, or measure signal from voltage indicators. Together these measurements offer unprecedented insight into the underlying source of the signal changes observed in fMRI. In addition, simultaneous measurements can be used to validate the application of graph theory approaches in the analysis of fMRI data. For example, approaches that extract dynamic connectivity components [Sakoĝlu2010, Chang2010, Hutchison2013] could be explicitly tested using the optical signal as a ground truth measure. Finally, this technology can be applied in neurological models of disease (e.g. post-traumatic stress disorder, depression, traumatic brain injury, autism etc.) to measure pathology and to test intervention strategies across spatiotemporal scales.

The mesoscopic Ca^{2+} imaging data can also be used as a stepping stone to connect BOLD contrast to single cell activity measurements. In a sister study to the present work, the same mesoscopic Ca^{2+} imaging method as presented here has been successfully combined with simultaneous 2-photon imaging of a small (typically $200\mu m^2$) cortical FOV. These simultaneous recordings measure the relationship between the activity of single cells and the patterns of cortical

activity observed on the mesoscale. Thus, together the combination of these studies span from the single cell to the whole brain.

In conclusion, the simultaneous imaging technology presented provides a tool that can be used to provide a firmer biological basis for understanding the functional organization of the brain in health and disease. With a direct link (fMRI signal) from mice to human subjects, fundamental insights will be obtained as to how the brain is functionally organized, and what are the contributions of different cell populations to the functional organizing principles observed.

METHODS

I. Surgical preparation

All procedures were performed in accordance with the Yale Institutional Animal Care and Use Committee (IACUC) and in agreement with the National Institute of Health Guide for the Care and Use of Laboratory Animals. All surgical materials are compatible with MRI. Anaesthesia is induced with 3% Isoflurane (1.5-2% during surgery). Fur is removed from the scalp and thigh (for MouseOx) using dilapidation cream (Nair™). Lidocaine (0.5%, Henry Schein Animal Health VINB-0024-6800) and marcaine/epinephrine (0.5%, Pfizer Injectables 00409175550) are used to numb the scalp prior to resection. Once the skull surface has been cleared of tissue, a dental cement (C&B Metabond®, Parkell) 'well' is built around the circumference of the skull surface; taking care not obstruct the Ca^{2+} imaging FOV. Dental cement is also used to secure the outside edges of the well to our in-house built head-plate (acrylonitrile butadiene styrene plastic, TAZ-5 printer, 0.35mm nozzle, Lulzbot) which cradles the sides of the skull and attaches above the olfactory bulb.

The head-plate dovetails with the MRI coil and Ca^{2+} imaging hardware to minimize motion and aid alignment. The well is filled with an optically transparent agar substitute: 0.5% Phytagel (BioReagent, CAS.71010-52-1) with 0.5% $MgSO_4$ in water, sealed with a glass cover-slip (Carolina Biological Supply Company, item.no.633029) and secured with dental cement. The well is necessary to avoid artifacts in the MRI data which are caused by neighboring materials with large differences in magnetic susceptibility (eg. a skull to air interface). Furthermore, the glass cover-slip provides a smooth surface which improves Ca^{2+} signal transmission. Care must be taken during the preparation to eliminate bubbles in the dental cement and Phytagel which cause artifacts in the MRI and Ca^{2+} data.

II. Optical components for the dual imaging experiment

Directly above the mouse, is a prism (25mm, uncoated, N-BK7, #32-336 RA-Prism, Edmund Optics) which redirects the excitation light (entering) and Ca^{2+} signal (exiting) by 90° such that they pass through the telecentric lens (MML-1-HR65DVI-5M, Moritex) which houses several optical components. For MRI compatibility, we replaced the stock telecentric lens metal housing with plastic (Derlin® Acetal Resin and PEEK, McMater-Carr). Furthermore, we replaced the beam-splitter within the telecentric lens with a dichroic lens (15x17x1mm, T495lpxr, Lot: 321390, CHROMA). Similarly, a custom plastic port which collimates (12 Dia. x 15 FL mm, VIS-EXT, Inked, Plano-Convex, Edmund Optics) and redirects the excitation light by 90° into the telecentric lens was custom built (Kramer Scientific). The excitation light arrives via a 5mmx5m liquid light guide (10-10645, Lumencor) from the room neighboring the magnet where the light source (Lumencor SPECTRA X, Lumencor) is housed. Similarly, a custom 4.6m x 14.5mm x 14.5mm coherent fiber optic bundle (N.A. 0.64) containing an array of 60μm multi-fibers (10μm elements, in a 6x6 array)

(SCHOTT Inc.), transports the Ca^{2+} signal to the room neighboring the magnet where the Ca^{2+} imaging data is recorded using a sCMOS camera (pco.edge 4.2). An additional green fluorescent protein (GFP) emission filter (ET525/50m, CHROMA) is placed between the optic fiber bundle and the camera connected by two optical extenders: a sub-assembly of rite 89 North TwinCam LS Image splitter (Cairn), to convert the focus plane for infinity focus.

III. Mice with genetically encoded Ca^{2+} indicators (TIGRE-1.0)

Mice were housed on a 12 hour light/dark cycle. Food and water were available ad libitum. Mice were adults, 6-8 weeks old, 25-30g, at the time of imaging. We report data from a first generation TIGRE (genomic locus) line crossed with reporter lines controlled by Cre recombinase (promoter) with a tetracycline-regulated transcriptional trans-activator (tTA) for amplification [Madisen2015, Zeng2008, Daigle2017, Harris2014]. These animals were selected because they have been shown to have high reporter and effect gene expression levels which translate to brighter Ca^{2+} signal; an important attribute for imaging within the magnet. For detailed expression level data refer to: http://connectivity.brain-map.org/transgenic;http://www.alleninstitute.org/what-we-do/brainscience/research/products-tools/ [Daigle2017].

Specifically, we report data from: Ai93 (or TIT2L-GCaMP6f, TIGRE - Insulators - TRE2 promoter - LoxPStop1LoxP - GFP CalModulin fusion Protein 6 fast), CaMK2a-tTA (CalModulin dependent protein Kinase 2 alpha), Slc17a7 (or Vglut1) - IRES (internal ribosome entry site) 2 - Cre mice purchased from Jackson Labs (JAX stock numbers: 024103, 003010 and 023517) and bred in-house. Slc17a7-Cre;Camk2a-tTA;Ai93 mice have GCaMP6f expression in excitatory neuronal cell populations.

IV. Functional imaging acquisition parameters

Ca^{2+} data is recorded at an effective rate of 10Hz. To enable frame-by-frame background correction (Methods, below V.), violet (395/25) and cyan (470/24) illumination is interleaved at a rate of 20Hz. The exposure time for each channel (violet/cyan) is 40ms to avoid artifacts caused by the rolling shutter refreshing. Thus, the sequence is as follows: 10ms blank, 40ms violet, 10ms blank, 40ms cyan etc.

fMRI data is acquired using a gradient-echo, echo-planar-imaging (EPI) sequence with a repetition time (TR) of 1 second, and an echo time (TE) of 9ms. The data are collected at a $0.4mm^3$ resolution, across 28 slices; yielding whole brain coverage. Each functional imaging run is 600 repetitions in length (10 minutes).

V. Ca^{2+} data processing

Images are rotated to align the anterior-posterior axis with vertical (MATLAB, *imrotate*). Violet and cyan frames, which are interleaved during data acquisition, are separated (odd/violet and even/cyan) and processed in parallel. Motion correction, using rigid body translation (MATLAB, *imregtform*), is performed on even/odd frames using a FOV containing fluorescent beads (not brain tissue) which are imbedded within the right-anterior dental cement (Fluorescent green PE microspheres, UVMS-BG-1.00, 106-125µm, Cospheric) Supplementary Figure 3.

Data are masked to isolate brain tissue (ImageJ, *polygon*). For even/odd frames, individual pixel baseline correction (MATLAB *imtophat,* line structure 300 width) is applied to remove the trend caused by photobleaching during the experiment. This results in a zero baseline. Data are baseline shifted back to the raw-data signal intensity by adding the average (pre-baseline

correction) signal of each pixel's time course back to each pixel. This is necessary for regression of the background signal (next step) and calculating the relative fluorescence change (final step). To remove non-GCaMP6f fluorescence changes (e.g. hemodynamic signal), we do background correction by regressing (MATLAB, *regress*) the violet from the cyan time course pixel-wise [Allen2016, Wekselblatt2017]. To compute the relative fluorescence change, each pixel in the background corrected (violet regressed from cyan) time course, is divided by the average signal of each pixel's time course. The result is the ΔF/F (F, fluorescence) movie (see Supplementary Figure 3 for raw and processed example movies, and motion estimates).

VI. fMRI data processing

Data are motion corrected (AFNI, Analysis of Functional NeuroImages, *3dVolReg*) [Cox1996], masked to isolate brain tissue (MATLAB, *roipoly*), and spatially blurred within the brain-mask (MATLAB, *smooth-gaussian*, full-width-half-maximum, FWHM, 0.8mm). The data are filtered (0.01-0.2Hz, MATLAB, *butterworth*), the global signal regressed (MATLAB, *detrend*), and the linear trend removed (MATLAB, *detrend*). Data with frame-wise motion estimates >0.4mm are excluded (voxel size 0.4mm^3). The majority of the data we collected contains sub-voxel motion (75% of evoked activity recordings and 82% spontaneous activity recordings, N=28/38) see Supplementary Figure 4.

VII. Structural MR-imaging parameters: data for multi-modal image registration

High in-plane resolution images of fMRI FOV. Using a multi-spin-multi-echo (MSME) imaging sequence. In 10 minutes 40 seconds, using a TR/TE of 2500/20ms, we obtain 28 slices (0.4mm thick) with a in-plane resolution of 0.1mm^2 (two averages). The slice prescription of these images matches those of the functional MR-images (i.e. they are of the same anatomy).

Isotropic 3D anatomy of the whole brain. Using a MSME imaging sequence. In 5 minutes 20 seconds, using a TR/TE of 5500/15ms, we obtain a 0.2mm^3 (single average) image of the whole brain. This sequence is repeated five times during our imaging protocol interleaved with functional acquisitions. Interleaving structural and functional acquisitions allows recovery of the Ca^{2+} signal and more robust responses to stimulation during functional data acquisitions with evoked responses. In post-processing, the five isotropic anatomical images are concatenated (MATLAB, *horzcat*), motion correct (AFNI, *3dVolReg*), and averaged (MATLAB, *mean*) to create one image.

MR-angiogram. Using a fast-low-angle-shot (FLASH) time-of-flight (TOF) imaging sequence. In 18 minutes, using a TR/TE of 130/4ms, we obtain a 0.05mm^3 2.0x1.0x2.5cm^3 image of the blood vessels within the cortex.

High resolution anatomy of angiogram FOV. Also using a FLASH sequence. In 7 minutes 30 seconds, using a TR/TE of 61/7.5ms, we obtain a 0.13x0.08x0.05mm^3 2.0x1.0x2.5cm^3 high resolution image of the anatomy within the same FOV as the MR-angiogram.

VIII. GLM for Ca^{2+} and BOLD responding ROIs to unilateral hind-paw stimulation

Ca^{2+} data. From each mouse, we collect 40 minutes of evoked responses to hind-paw stimulation during four 10 minute sessions which are interspersed between spontaneous activity recordings and structural imaging. Preprocessed Ca^{2+} data containing evoked responses are normalized (MALTAB, *zscore*) and fit using a GLM (MATLAB, *glmfit*). Motion parameter estimates from simultaneously recorded fMRI data, a drift parameter (photobleaching), motion estimates from

fluorescent beads (Supplementary Figure 3), as well as a box-car response function are included in the model. The response map is thresholded for pixels with beta values larger than the FWHM beta value. Clusters with <30 pixels are discarded (MATLAB, *bwconncomp*). Similar ROI results are obtained when motion estimates and/or drift parameters are not included within the model.

BOLD data. Data containing evoked responses are fit using a GLM (AFNI, *3dDeconvolve*). Drift and motion parameters as well as a custom hemodynamic response function (HRF) are included in the model. The HRF is derived from the average evoked response recorded from a mouse imaged during a pilot experiment (not one of the N=6 reported in Results). See Supplementary Material II. for the derivation of the HRF. The response map is thresholded to correct for multiple comparisons (false discovery rate q<0.01) and a limit for cluster size (>30 contiguous voxels) applied.

IX. Ca^{2+} and BOLD signal parcellation by applying multi-graph k-way clustering

We denote the original data set (either Ca^{2+} or BOLD) as $\left\{F_k\right\}_{k=1}^{K}$, where *k* can be the index for different time points from one animal or the index for different animals. Each F_k is organized as a 2D matrix $F_k = \left[f_{1k} f_{2k} \ldots f_{ik} \ldots f_{Nk}\right]$, where each column is a time course indexed by *i*, and *N* is the total number of pixels (2D, Ca^{2+} data) or voxels (3D, fMRI data).

To apply the clustering algorithm, we construct a graph $\mathcal{G}_k$ for each set of data in F_k. The graph consists of vertices and edges. Vertices are the *N* pixels/voxels and edges are the connections between each pair of vertices. Edges are characterized by their strength, which is quantified by measuring the similarity between the time courses of pairs of vertices. Accordingly, we calculate a matrix of weights W_k of size *N* x *N* for a given F_k, and each entry w_{ij} is defined by $w_{ij} = exp\left(\frac{-d_{ij}^2}{2*\sigma^2}\right)$. Here, we define $d_{ij}^2 = 2*(1 - r_{ij})$, where r_{ij} is the Pearson correlation between the time course of pixel/voxel *i* and pixel/voxel *j*.

The optimization and computation of the clustering algorithm is performed in the spectral domain. In other words, given a W_k, we compute the first *m* eigenvectors of W_k denoted as $X_k = \left[x_{1k} x_{2k} \ldots x_{mk}\right]$, X_k is of size *N* x *m*, and each column is an eigenvector. The multi-graph k-way clustering algorithm is then set to solve the following optimization,

$$minimizing \phi\left(Y, \left\{R_k\right\}\right) = \sum_k \left\|Y - X_k R_k\right\|^2$$

$$subject to Y \in \{0,1\}^{N \times m}, Y 1_m = 1_N, and R_k^T R_k = I_m$$

where *Y* is the *m*-ROI parcellation of the brain based on the total *K* time courses, 1_N is a single column vector of size *N*, and I_m is the *m x m* identity matrix. The optimization is solved iteratively. For more details refer to Shen et al. 2013 [Shen2013] . After *Y* is solved, we convert *Y* to a 1D label. Each row of *Y* corresponds to one pixel/voxel. By definition, each row of *Y* has one out of *m* entries equal to one, and all other *(m-1)* entries are zero. Thus, the label for each pixel/voxel *i* is the column index where the ith row of *Y* equals is one. Finally, the 1D label is mapped to the original 2D/3D space for visualization and further analysis. See Supplementary Figure 9.

REFERENCES

1. Ogawa S, Tank DW, Menon R, Ellermann JM, Kim SG, Merkle H, Ugurbil K. Intrinsic signal changes accompanying sensory stimulation: functional brain mapping with magnetic resonance imaging. *Proc Natl Acad Sci. U.S.A.* 1992: 89:5951–5955.
2. Schulz K, Sydekum E, Krueppel R, Engelbrecht CJ, Schlegel F, Schröter A, Rudin M, Helmchen F. Simultaneous BOLD fMRI and fire-optic calcium recording in rat neocortex. *Nat Methods.* 2012; 9(6): 597-602.
3. Liang Z, Ma Y, Watson GDR, Zhang N. Simultaneous GCaMP6-based fiber photometry and fMRI in rats. *J Neurosci Methods.* 2017; 289: 31-38.
4. Schwalm M, Schmid F, Waschsmuth L, Backhaus H, Kronfeld A, Aedo Jury F, Prouvot PH, Fois C, Albers F, van Alst T, Faber C, Stroh A. Cortex-wide BOLD fMRI activity reflects locally-recorded slow oscillation-associated calcium waves. Elife. 2017; 6; e27602.
5. Albers F, Wachsmuth L, van Last TM , Faber C. Multimodal functional neuroimaging by simultaneous BOLD fMRI and fibre-optic calcium recordings and ontogenetic control. *Mol Imaging Biol*. 2018; 20(2): 171-182.
6. Schlegel F, Sych Y, Schroeter A, Stobart J, Weber B, Helmchen F, Rudin M. Fibre-optic implant for simultaneous fluorescence-based calcium recordings and BOLD fMRI in mice. *Nat Protoc*. 2018; 13(5):840-855.
7. Wang M, He Y, Sejnowski TJ, You X. Brain-state dependent astrocytic Ca^{2+} signals are coupled to both positive and negative BOLD-fMRI signals. *Proc Natl Acad Sci USA.* 2018; 115(7): E1647-E1656.
8. Murphy MC, Chan KC, Kim SG, Vazquez AL. Macroscale variation in resting-state neuronal activity and connectivity assessed by simultaneous calcium imaging, hemodynamic imaging and electrophysiolocy. *Neuroimage.* 2018; 169: 352-362.
9. Gu X, Chen W, You J, Koretsky AP, Volkow ND, Part Y, Du C. Long-term optical imaging of neurovascular coupling in mouse cortex using GCaMP6f and intrinsic hemodynamic signals. *Neuroimage.* 165; 251-264.
10. Ma Y, Shaik MA, Kozberg MG, Kim SH, Portes JP, Timerman D, Hillman EM. Resting-state hemodynamics are spatiotemporally coupled to synchronized and symmetric neural activity in axcitatory neurons. *Proc Natl Acad Sci USA.* 2016; 113(52): E8463-E8471.
11. Hillman EMC. Coupling mechanism and significance of the BOLD signal: A status report. *Annu Rev Neurosci.* 2014; 37: 161-181.
12. Shen X, Papademetris X, Constable RT. Graph-theory based parcellation of functional subunits in the brain from resting-state fMRI. *Neuroimage.* 2010; 50(3):1027-1035.
13. van Oort ESB, Mennes M, Navarro Schröder T, Kumar VJ, Zaragoza NI, Grodd W, Doeller CF, Beckmann CF. Functional parcellation using time courses of instantaneous connectivity. *Neuroimage.* 2018; 170: 31-40.
14. Arslan S, Ktena SI, Makropouluos A, Robinson EC, Rueckert D, Parisot S. Human brain mapping: A systematic comparison of parcellation methods for the human cerebral cortex. *Neuroimage.* 2018; 170: 5-30.
15. Eickhoff SB, Yeo BTT, Genon S. Imaging-based parcellation son the human brain. *Nat Rev Neurosci.* 2018; 19(11):672-686.
16. Shen X, Tokoglu F, Papademetris X, Constable RT. Groupwise whole-brain parcellation from resting-state fMRI data for network node identification. *Neuroimage.* 2013; 82:403-15.
17. Buckner RL, Sepulcre J, Talukdar T, Krienen FM, Liu H, Hedden T, Andrews-Hanna JR, Spering RA, Johnson KA. Cortical hubs revealed by intrinsic functional connectivity: Mapping,

assessment of stability, and relation to Alzheimer's disease. J *Neruoscience*. 2009; 29(6): 1880–1893.
18. Brown J, Terashima K, Burggren A, Ercoli L, Miller K, Small G, Bookheimer S. Brain network local interconnectivity loss in aging APOE-4 allele carriers. *Proc Natl Acad Sci USA*. 2011; 108: 20760–20765.
19. Cao H, Xu X, Zhao Y, Long D, Zhang M. Altered brain activation and connectivity in early Parkinson disease tactile perception. *AJNR Am J Neuroradiol*. 2011; 32: 1969–1974.
20. Yao Z, Zhang Y, Lin L, Zhou Y, Xu C, Jian T. Abnormal cortical networks in mild cognitive impairment and Alzheimer's disease. *PLoS Computat Biol*. 2010: 6(11): e1001006.
21. Sanz-Arigita E, Schoonheim M, Damoiseaux J, Rombouts S, Maris E, Barkhof F, Scheltens P, Stam C. Loss of 'small world' networks in Alzheimer's disease: graph analysis of fMRI resting-state functional connectivity. *PLoS One*. 2010: 5(11): e13788.
22. Wang L, Hermens D, Hickie I, Lagopoulos J. A systematic review of resting-state functional-MRI studies in major depression. *J of Affect Disord*. 2012; 142(1-3): 6–12.
23. Anticevic A, Brumbaugh M, Winkler A, Lombardo L, Barrett J, Corlett P, Kober H, Gruber J, Repovs G, Cole M, Krystal J, Pearlson G, Glahn D. Global prefrontal and fronto-amygdala dysconnectivity in bipolar disorder with psychosis history. *Biol Psychiatry.* 2013 73(6): 565-573.
24. Venkataram A, Whitford T, Westin C, Golland P, Kubicki M. Whole brain resting state functional connectivity abnormalities in schizophrenia. *Schizophr Res*. 2012; 139(1-3): 7–12.
25. Craddock RC, James GA, Holtzheimer PE 3rd, Hu XP, Mayberg HS. A whole brain fMRI atlas generated via spatially constrained spectral clustering. *Hum Brain Mapp.* 2012; 33(8): 1914-1928.
26. Daigle TL, Madisen L, Hage TA, Valley MT, Knoblich U, Larsen RS, et al. A suite of transgenic driver and reporter mouse lines with enhanced brain cell type targeting and functionality. *bioRxiv.* 2017: 224881; doi: https://doi.org/10.1101/224881
27. Madisen L, Garner AR, Shimaoka D, Chuong AS, Klapoetke NC, Li L, et al. Transgenic mice for intersectional targeting of neural sensors and effectors with high specificity and performance. *Neuron.* 2015; 85(5): 942–958.
28. Zeng H, Horie K, Madisen L, Pavlova MN, Gragerova G, Rohde AD, et al. An inducible and reversible mouse genetic rescue system. *PLoS Genet.* 2008; 4(5): e1000069.
29. Harris JA, Hirokawa KE, Sorensen SA, Gu H, Mills M, Ng LL, et al. Anatomical characterization of Cre driver mice for neural circuit mapping and manipulation. *Front Neural Circuits*. 2014; 8: 76.
30. Wekselblatt JB, Flister ED, Piscopo DM, Niell CM. Large-scale imaging of cortical dynamics during sensory perception and behavior. *J Neurophysiol.* 2016; 115(6): 2852-2866.
31. Allen WE, Kauvar IV, Chen MZ, Richman EB, Yang SJ, Chen K, et al. Global representation fo goal-directed behaviorin distinct cell types of mouse neocortex. *Neuron.* 2017; 94(4): 891-907.
32. Cox RW. AFNI: software for analysis and visualization of functional magnetic resonance neuroimages. *Comput Biomed Res*. 1996; 29,162-73.
33. Studholme C, Hill DL, Hawkes DJ. Automated 3-D registration of MR and CT images of the head. Med Image Anal. 1996; 1(2), 163-175.
34. Ruckert D, Sonoda LI, Hayes DL, Leach MO, Hawkes DJ. Nonrigid registration using free-form deformations: application to breast MR images. IEEE Trans Med Imaging. 1999; 18(8), 712-721.
35. Papademetris X, Jackowski AP, Schultz RT, Staib LH, Duncan JS. Non-rigid Brain Registration using Extended Robust Point Matching for Composite Multisubject fMRI Analysis. MICCAI 2003; 2, 788-795.

36. Markelja P, Tomaževiča D, Likara, B, Pernuša F. A review of 3D/2D registration methods for image-guided interventions. Medical Image Analysis, 2012; 16(3): 642-661.
37. Schulz K, Sydekum E, Krueppel R, Engelbrecht CJ, Schlegel F, Schröter A et al. Simultaneous BOLD fMRI and fibre-optic calcium recording in rat neocortex. Nat Methods. 2012; 9(6): 597-602.
38. Gao YR, Ma Y, Zhang Q, Winder AT, Liang Z, Antinori L, Drew PJ, Zhang N. Time to wake up: Studying neurovascular couling and brain-wide circuit function in the un-anesthetized animal. *Neuroimage.* 2017; 153: 382-398.
39. Sakoĝlu U, Pearlson GD, Kiehl KA, Wang YM, Michael AM, Calhoun VD. A method for evaluating dynamic functional network connectivity and task-modulation: application to schizophrenia. *MAGMA.* 2010; 23(5-6): 351-366.
40. Chang C, Glover GH. Time-frequency dynamics of resting-state brain connectivity measured with fMRI. *Neuroimage.* 2011; 50(1): 81-98.
41. Hutchison RM, Womelsdorf T, Allen EA, Bandettini PA, Calhoun VD, Corbetta M et al. Dynamic functional connectivity: promise, issues and interpretations. *Neuroimage.* 2013; 80: 360-378.

Figure 1. Experimental set-up for simultaneous mesoscopic Ca^{2+} and MR-imaging

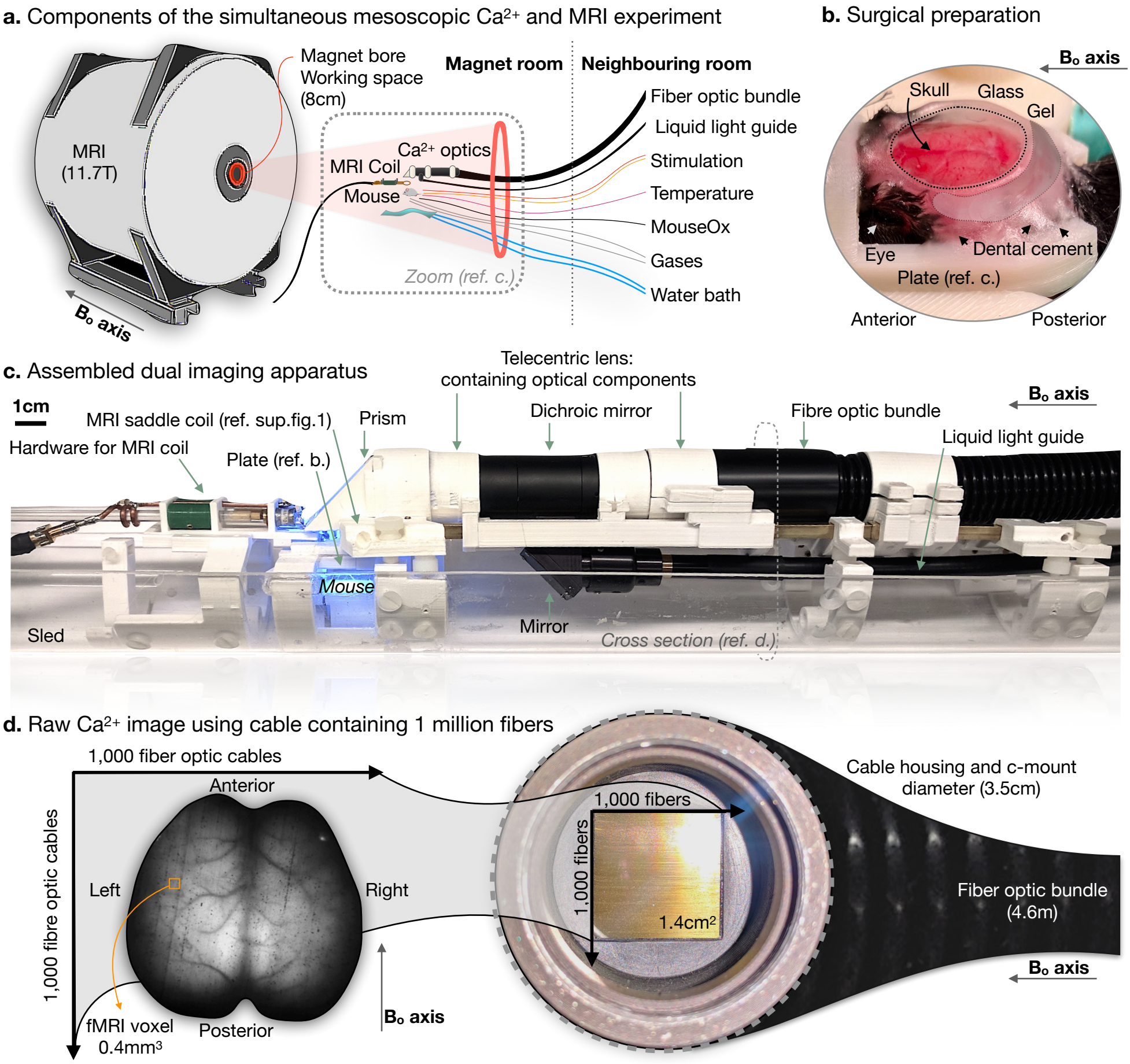

Figure 1. Experimental set-up for simultaneous mesoscopic Ca^{2+} and MR-imaging. An overview of the components (a.). Housed within the magnet room is an 11.7T MR-scanner with an 8cm bore diameter. Within this space, we insert the optical components for Ca^{2+} signal acquisition, MRI coil, animal, and physiological monitoring and maintenance equipment. The room neighbouring the magnet houses equipment which must be shielded from the high magnetic field. The Ca^{2+} signal is collected through an intact skull. Thus, a minimally invasive surgical preparation is necessary. A photograph of a prepared animal (b.). Following resection of the scalp and tissue overlying the skull surface, a 'well' of dental cement is created around the circumference of the cleaned skull. The well is filled with optically transparent Phytagel and sealed with a glass cover-slip. This minimizes susceptibility artifacts in MR-images and provides a smooth surface which improves Ca^{2+} signal transmission. The preparation is secured to a plate which cradles the sides of the skull and attaches above the olfactory bulb. The plate is fixed to the MRI coil below the Ca^{2+} imaging hardware. A photograph of the assembled dual imaging apparatus (c.). The Ca^{2+} imaging data is recorded by a CCD camera housed in the room neighbouring the magnet. A 4.6m fiber optic bundle relays the Ca^{2+} signal from within the magnet to the neighbouring room. For a whole cortex FOV, we use a fiber optic bundle containing 1 million fibers. A photograph of the fiber bundle, as well as a raw Ca^{2+} image captured using our set-up (d.).

Figure 2. Registration pipeline for simultaneously acquired Ca^{2+} and MRI data

a. Different Ca^{2+} and MRI fields of view

i. Ca^{2+} captures a 2D surface

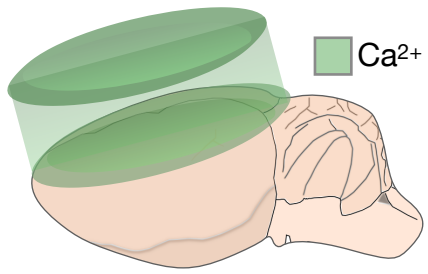

Example (ref. c.iii)

ii. MRI captures a 3D volume

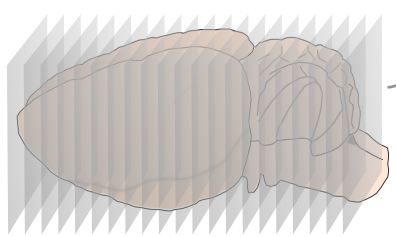

Anterior Posterior

iii. Example unprocessed coronal functional and structural MR imaging data

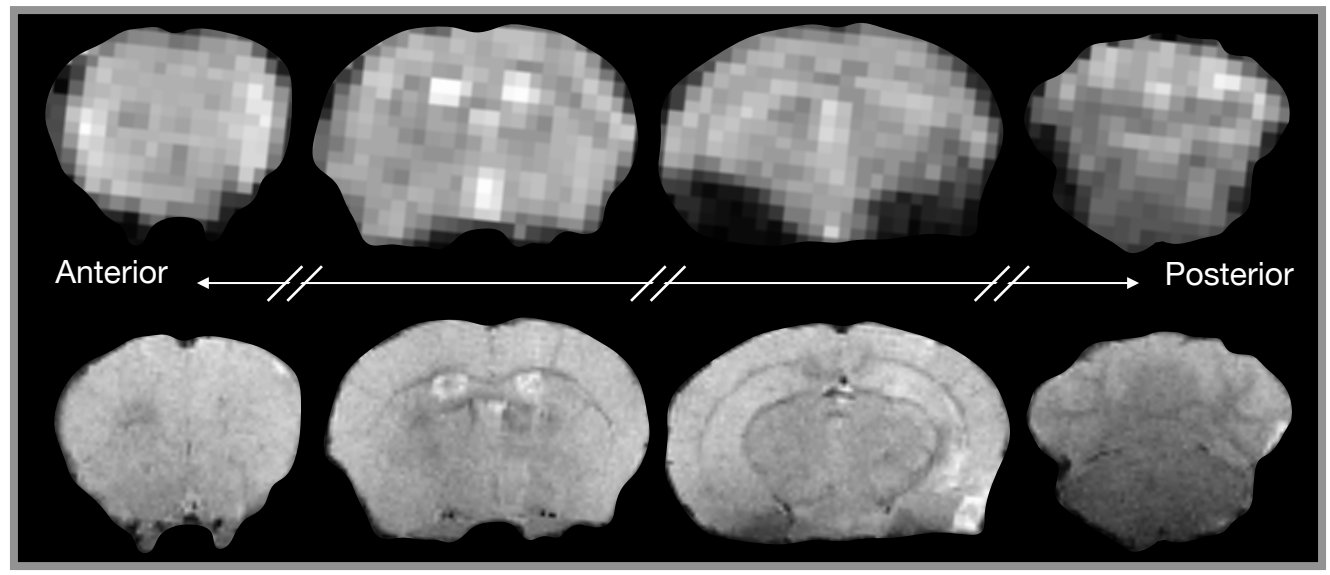

b. Overview of multi-modal image registration algorithm (numbers referenced in online methods IV. and VII.)

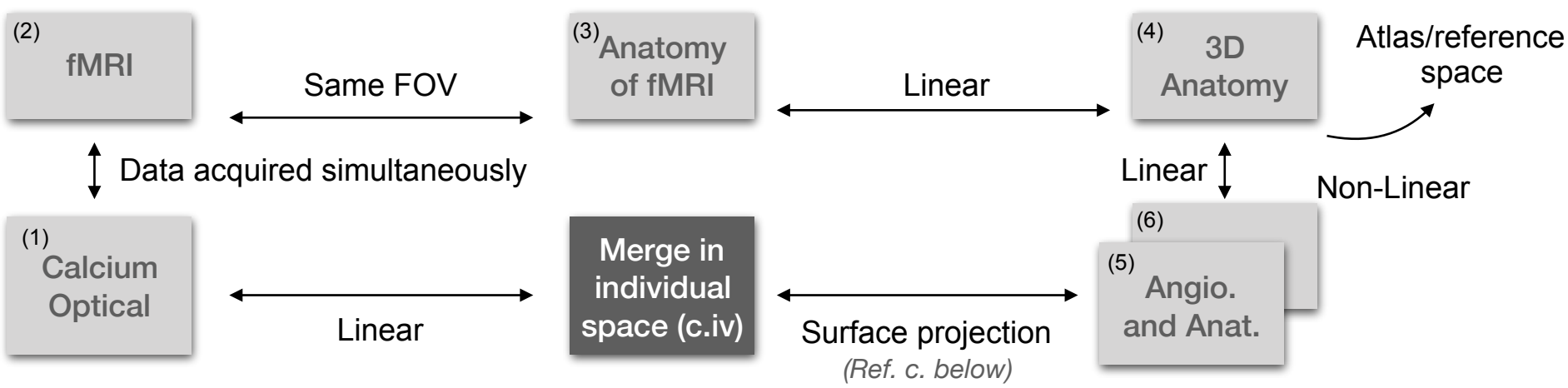

c. Ca^{2+} and MRI data registration using surface vessels as anatomical landmarks

i. MR angioram maximum intensity projection

ii. MR surface projection

iii. Average Ca^{2+} image

iv. Merge of MRI and Ca^{2+} data

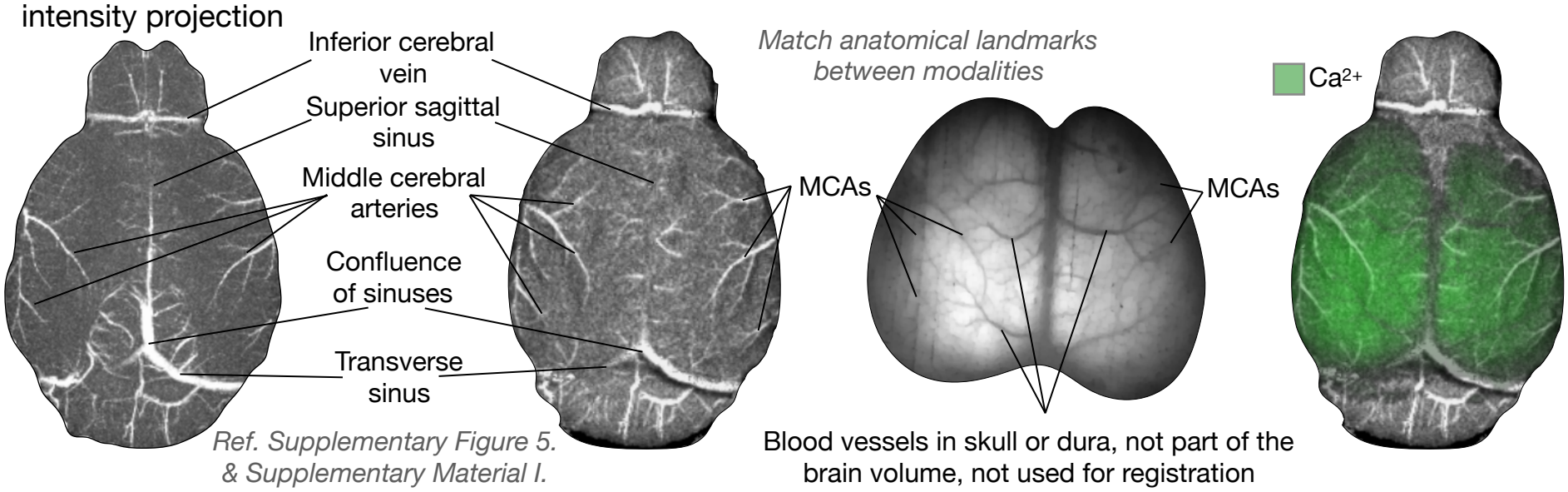

Figure 2. Registration pipeline for simultaneously acquired Ca^{2+} and MRI data. The registration of Ca^{2+} and fMRI data is non-trivial because the Ca^{2+} data is a 2D view of the cortical surface (tissue depth contributing to the signal is unknown), and the functional MRI data is a 3D volume. Cartoons depicting the Ca^{2+} (**i.**) and functional MRI (**ii.**) FOV are shown in (**a.**). Example MR functional (top row) and structural (bottom row) images are shown in (**a.iii.**). For multi-modal image registration (**b.**), in addition to the Ca^{2+} (1) and fMRI (2) simultaneously acquired data, we acquire: a high in-plane resolution image of the fMRI FOV (3), an isotropic 3D anatomical image of the whole brain (4), an MR-angiogram (5), and a high resolution anatomical image of the angiogram FOV (6). Using a rigid registration algorithm the functional and structural MRI data are registered in 'individual space'. Non-linear registration is used to register each individual mouse to an atlas or reference space. To register the Ca^{2+} and MRI data (**c.**), we begin by using a custom ray-casting algorithm (ref. Supplementary Figure 5. & Supplementary Material I.) on the MR-angiogram data (**c.i.**) to create a surface projection (**c.ii.**). Surface vessels (e.g. projections from the middle cerebral arteries) and anatomical features (e.g. midline) visible in the MR-surface projection and the average Ca^{2+} image (**c.iii.**) are used to move the Ca^{2+} and MRI-data to the same space (merged image, **c.iv.**).

Figure 3. Spontaneous fluctuation in the magnitude of evoked Ca^{2+} and BOLD responses are correlated

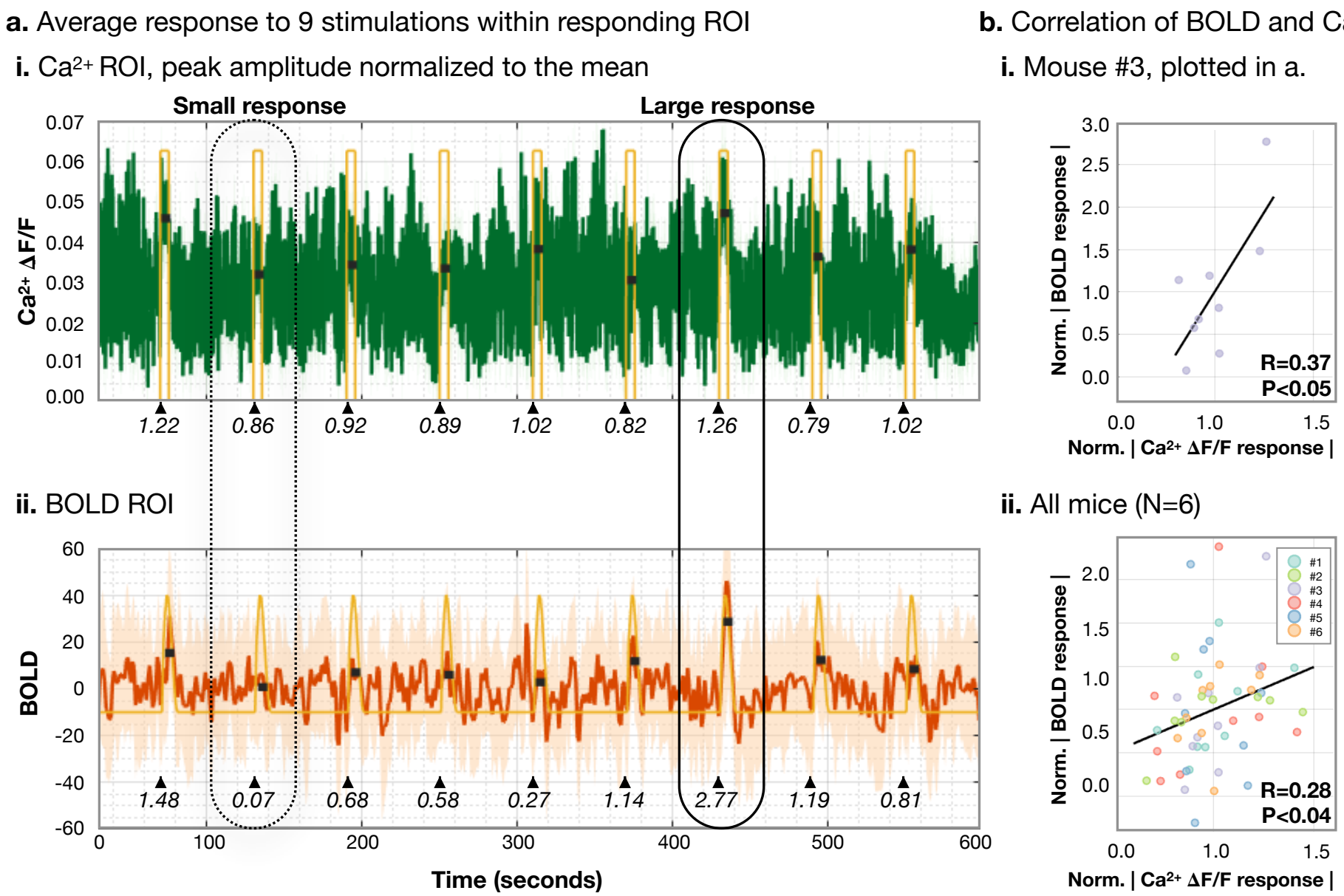

Figure 3. Spontaneous fluctuations in the magnitude of evoked Ca^{2+} and BOLD responses are correlated. The average response within the responding ROI of the Ca^{2+} (green) (**a.i.**) and BOLD (orange) (**a.ii.**) data for an example mouse are plotted for one 10 minute experiment: N=9 responses. For reference, the box-car (**i.**) and HRF (**ii.**) from the GLMs are plotted in yellow. During data recording there are spontaneous fluctuations in the magnitude of the Ca^{2+} and BOLD responses. An example small (dashed line) and large (solid line) amplitude response are circled. We estimate peak amplitude response by averaging the signal from the peak until three seconds after the peak (each stimulus is 5 seconds long). The time of the peak was calculated (ref. Supplementary Figure 8). The three second periods for each peak are shown by black lines at the level of each estimated response. The normalized response amplitude (to mean signal) is written beneath each response (below black triangles which denote stimulus onset time). For the example mouse (plotted in **a.**), across the N=9 presented stimuli, the normalized Ca^{2+} and BOLD response amplitudes are correlated (MATLAB, *corr*) R=0.37 P<0.05 (**b.i.**). Across all mice, N=6, (N=9 responses per mouse) we find the same relationship R=0.28, P<0.04 (**b.ii.**).

Figure 4. Stability of connectivity using Ca^{2+} and BOLD data parcellation

a. Representative Ca^{2+} parcellation results

† *parcellation corresponding to connectivity plotted in c.*

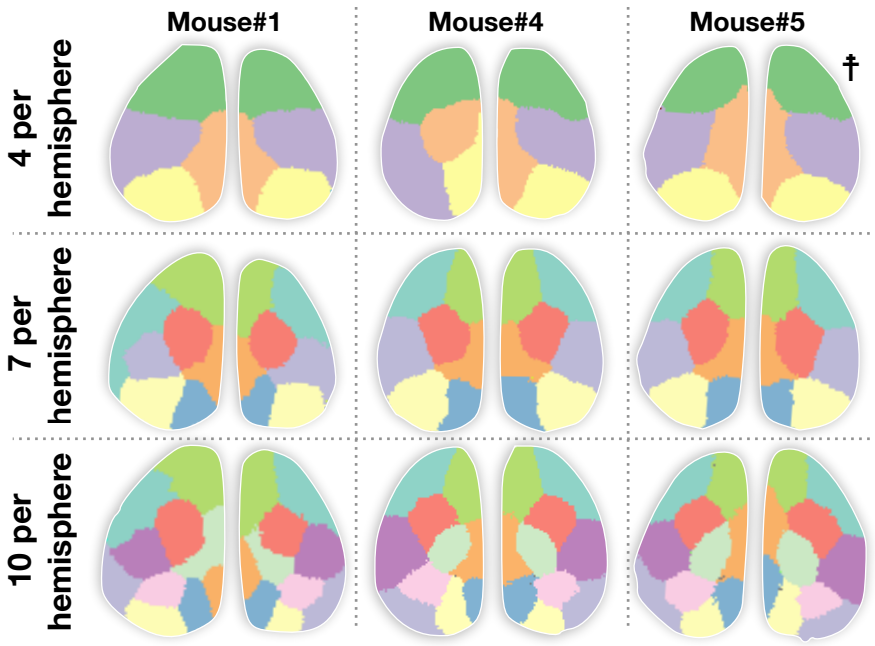

b. Representative BOLD parcellation results

† *parcellation corresponding to connectivity plotted in d.i.*

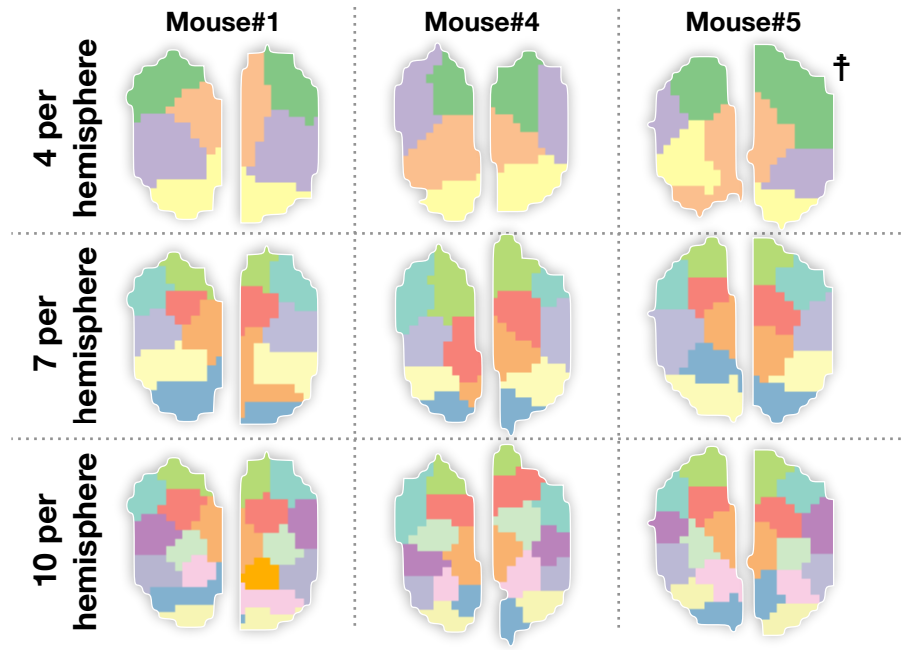

c. Correlation strength of edges during five runs of spontaneous activity Ca^{2+} data collection

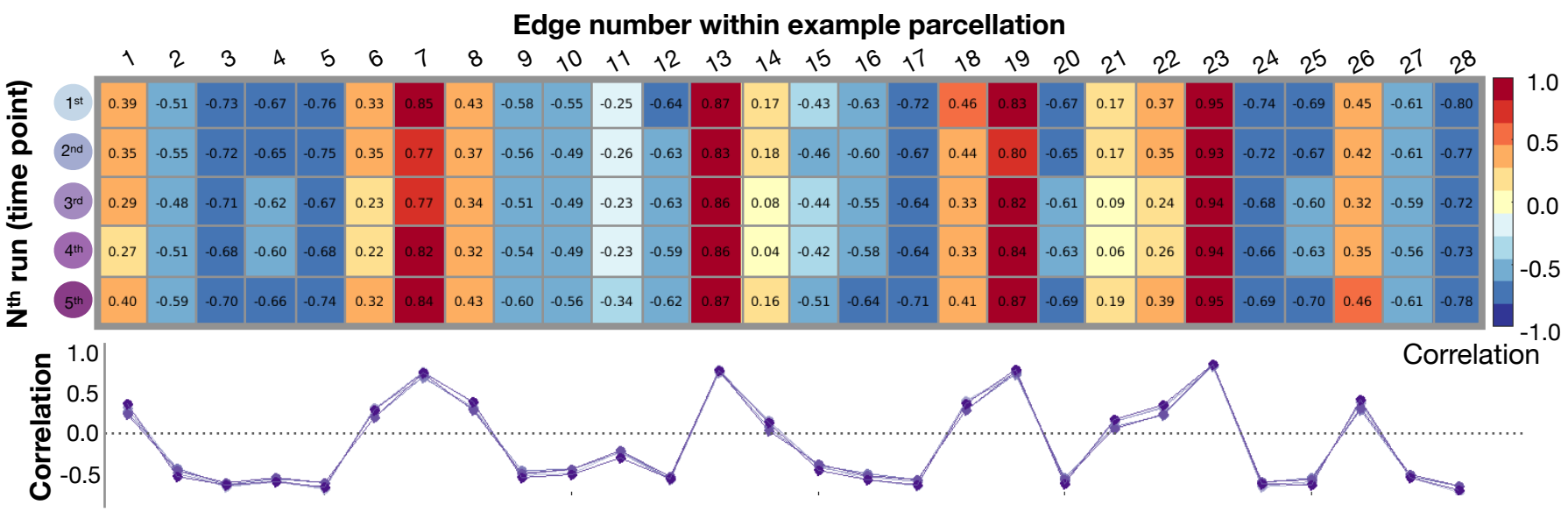

d. Correlation strength of edges during five runs of spontaneous activity BOLD data collection

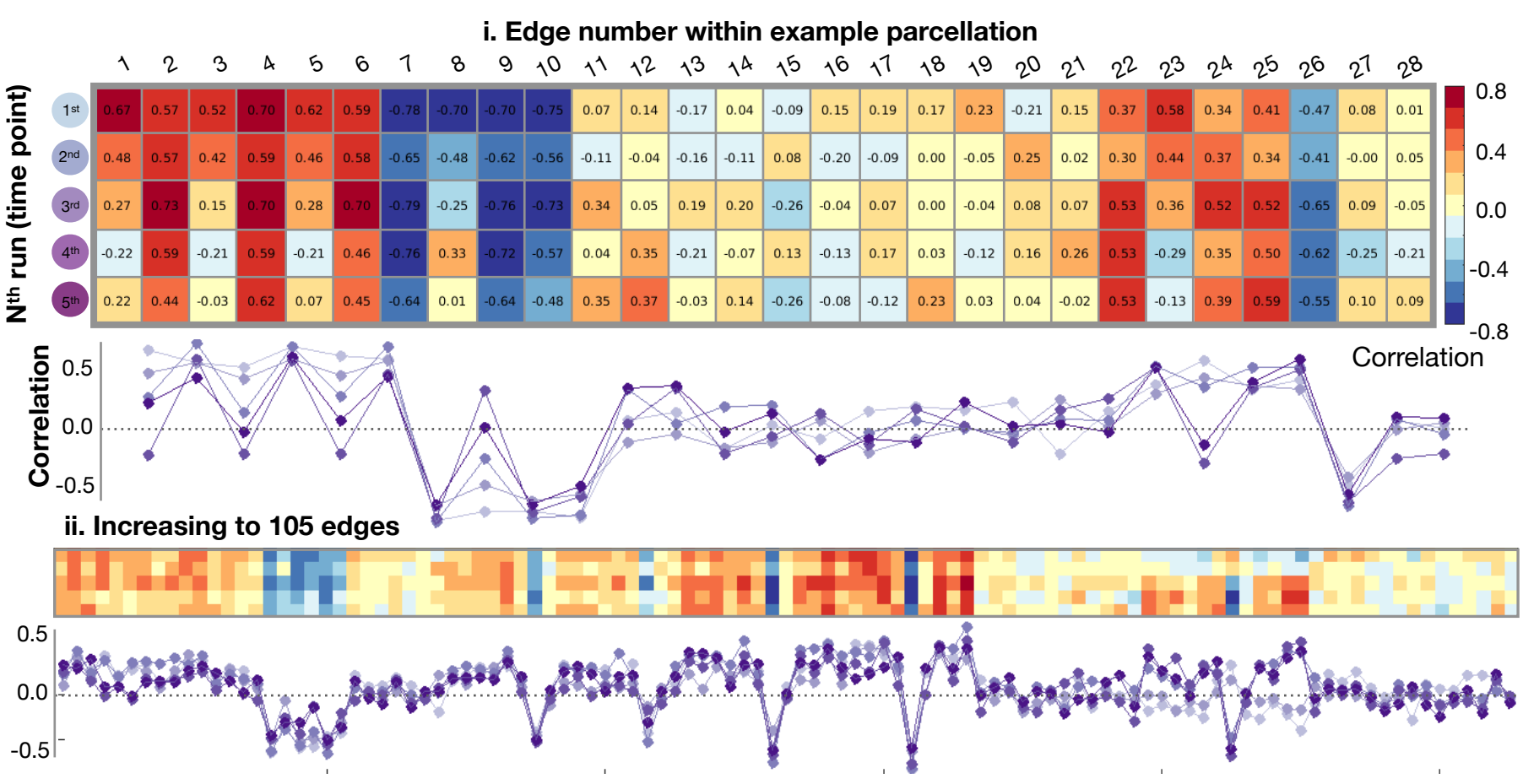

Caption next page.

Figure 4. Stability of connectivity using Ca^{2+} and BOLD data parcellation. Using multi-graph k-way clustering (Online Methods IX.), Ca^{2+} (a.) and BOLD (b.) data are parcellated. Three example animals choosing the number of parcels ('m') to be either 4, 7 or 10 per hemisphere. Data from each hemisphere is analyzed separately. Thus, symmetry between hemispheres indicates that the algorithm finds the expected bilateral pattern. Furthermore, similarity between parcellations across modalities indicates the presence of shared spatial features between modalities. This is examined explicitly in the next section. Finally, survival of boarders (by the subdivision of large into small parcels) as the number of parcels increases (from 4 to 7 to 10) - in place of the redrawing of new parcels across boarders - indicates reproducibility. In (b.) and (c.) we compute the stability of connectivity patterns throughout the experiment. Ten minutes of spontaneous activity is recorded at five time points which span the imaging protocol. We calculate connectivity between each pair of regions (i.e. connectivity strength along edges) using Pearson correlation. The complete set of edge strengths can be expressed as a vector. For one Ca^{2+} (c.) and two BOLD (d.) example parcellations, we show these vectors assembled into matrices of edges by time points. Below each matrix, a scatterplot of connectivity strength by edge for each time point (purple). The connectivity profile (the pattern of high and low edge strengths) is preserved across time. For 8-10 parcels per hemisphere, connectivity stability is very high: Ca^{2+} $R=0.995 \pm 0.003$, and BOLD $R=0.84 \pm 0.09$.

Figure 5. Parcellation of Ca^{2+} and BOLD spontaneous activity data

a. Representative Ca^{2+} and BOLD parcellation results transposed between Ca^{2+} and BOLD space

i. Parcellation on Ca^{2+} data

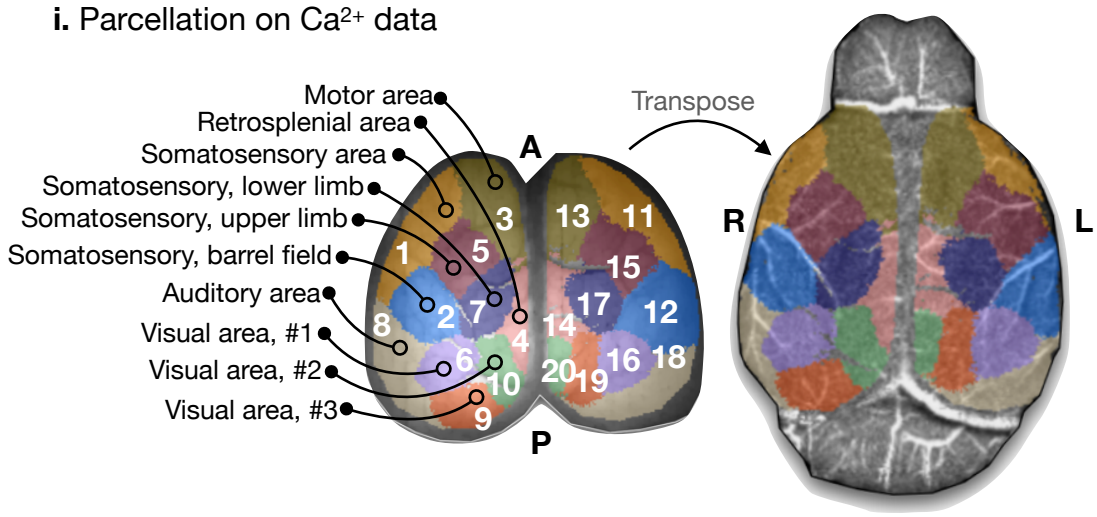

ii. Parcellation on BOLD data

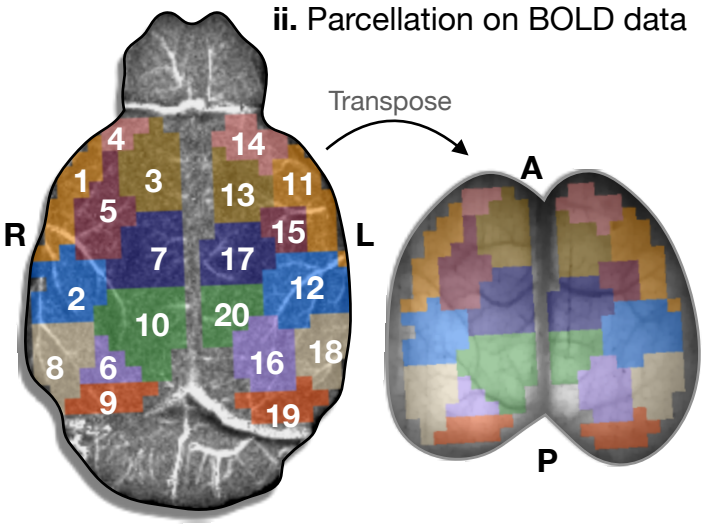

b. Average (N=6) Ca^{2+} and BOLD connectivity matrices

i. Parcellation on Ca^{2+} data

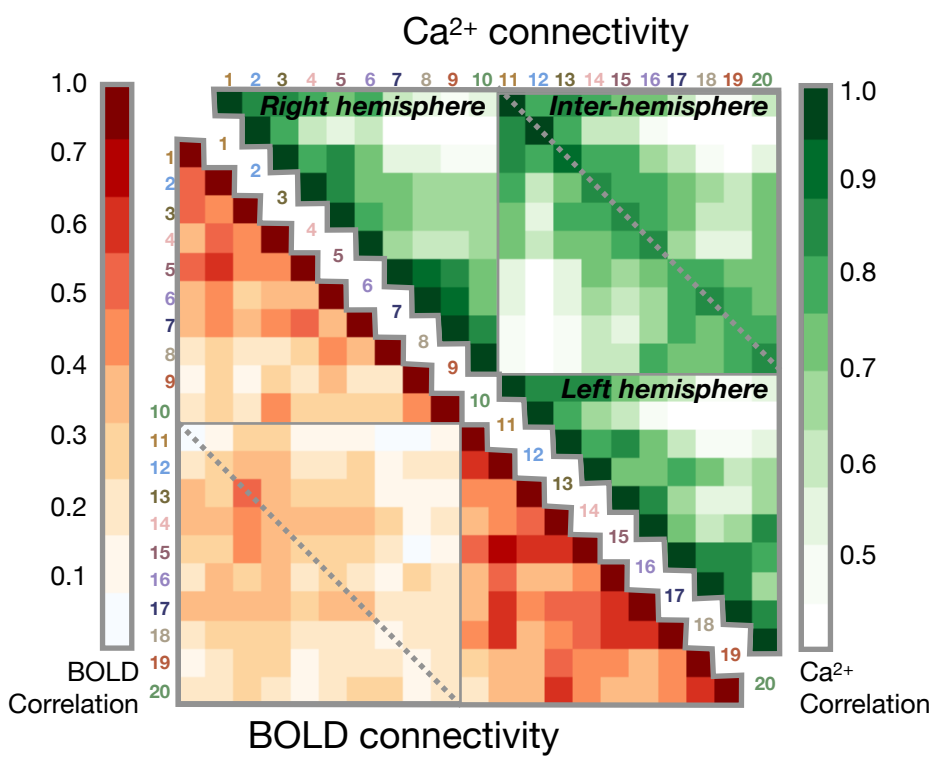

i. Parcellation on BOLD data

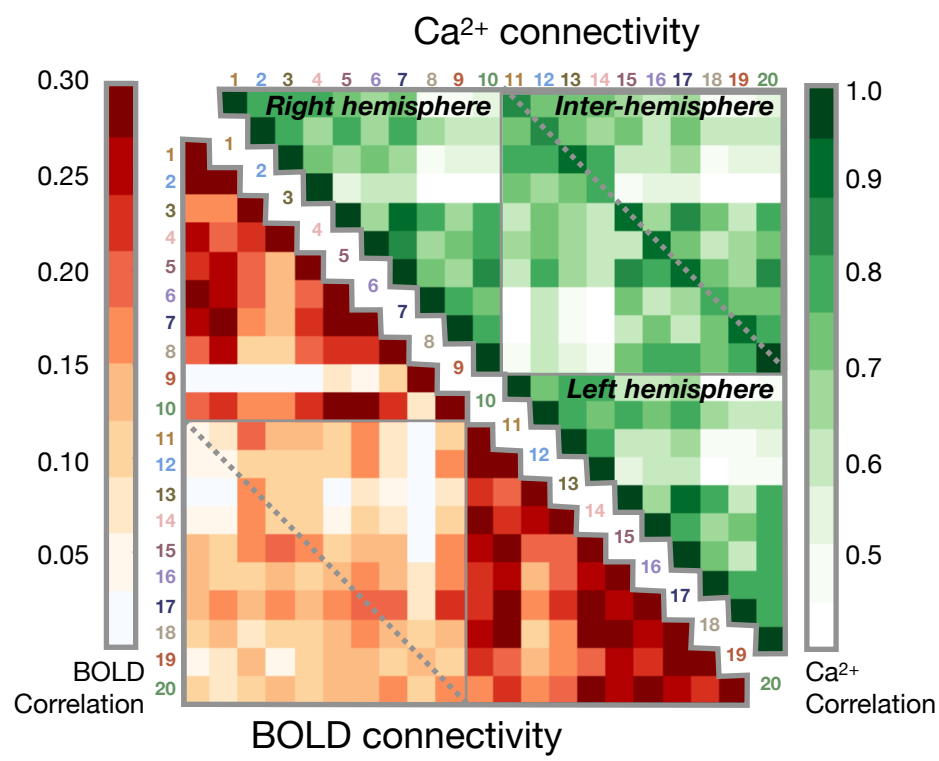

c. Average (N=6) connectivity measured in Ca^{2+} and BOLD data using Ca^{2+} and BOLD parcellations

i. Parcellation on Ca^{2+} data

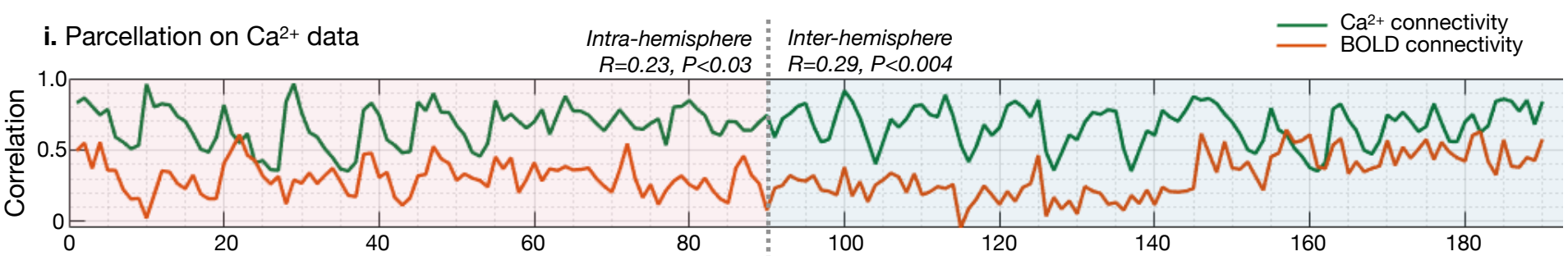

ii. Parcellation on BOLD data

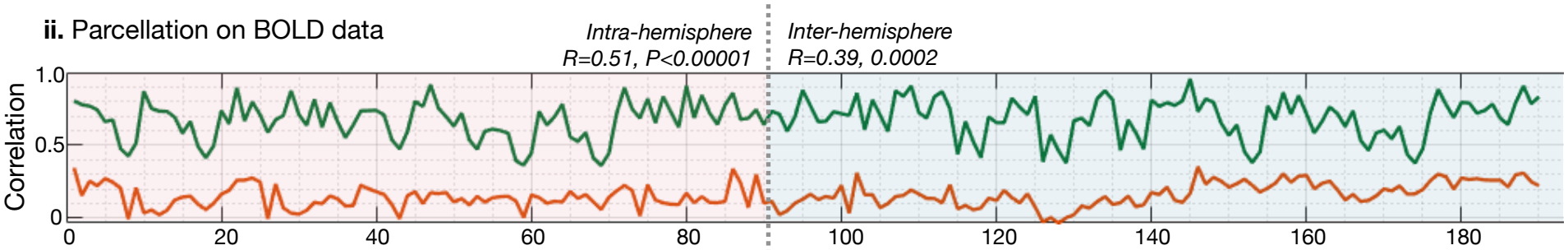

Edge number within parcellation (10 parcels per hemisphere)

Caption next page.

Figure 5. Parcellation of Ca^{2+} and BOLD spontaneous activity data. For all mice (N=6) a functional parcellation of the Ca^{2+} and BOLD data is computed. The Ca^{2+} parcellation can be projected (or transposed) onto the BOLD data. Likewise, the BOLD parcellation can be transposed onto the Ca^{2+} data. In (a.i.), an example Ca^{2+} parcellation in native Ca^{2+} space as well as transposed into BOLD space is shown. Likewise, in (a.ii.), an example BOLD parcellation in native BOLD space as well as transposed into Ca^{2+} space is shown. The ROIs identified within the parcellation are named based on proximity to regions within the Allen atlas (ref. Supplementary Figure 10), with the exception of the somatosensory lower limb area which can reliably be identified by evoked responses. In (b.), the average (N=6) Ca^{2+} (green, upper right) and BOLD (red, lower left) connectivity matrix for the Ca^{2+} (b.i.) and BOLD (b.ii.) parcellations. In (c.), the similarity of Ca^{2+} and BOLD connectivity strength is quantified. For the Ca^{2+} (c.i.) and BOLD (c.ii.) parcellations, the average Ca^{2+} (green) and BOLD (orange) connectivity strength is plotted. Intra-hemisphere (shaded in pink), inter-hemisphere (shaded in blue), and whole brain Ca^{2+} and BOLD connectivity are correlated. In other words, regions identified by either Ca^{2+} or BOLD based parcellation which show high/low synchrony in Ca^{2+} also show high/low synchrony in BOLD.